Light sheet fluorescence microscopy for *in situ* cell interaction analysis in mouse lymph nodes

Jun Abe[1,7], Aleksandra J. Ozga[1,7], Jim Swoger[2,3], James Sharpe[2,3,4], Jorge Ripoll[5,6,8], Jens V. Stein[1,8]

[1] Theodor Kocher Institute, University of Bern, 3012 Bern, Switzerland

[2] MBL/CRG Systems Biology Research Unit, Centre for Genome Regulation (CRG), 08003 Barcelona, Spain

[3] Universitat Pompeu Fabra (UPF), 08002 Barcelona, Spain

[4] Institució Catalana de Recerca i Estudis Avançats (ICREA), 08010 Barcelona, Spain

[5] Universidad Carlos III of Madrid, Department of Bioengineering and Aerospace Engineering, Madrid 28911, Spain

[6] Experimental Medicine and Surgery Unit, Instituto de Investigación Sanitaria del Hospital Gregorio Marañón, 28007 Madrid, Spain

[7] Co-first authors

[8] Co-corresponding authors

Contact: Jorge Ripoll

Dept. of Bioengineering and Aerospace Engineering

Universidad Carlos III of Madrid

Avda. de la Universidad 30,

28911 Leganés, Madrid

Spain

Tel:+34 91 6248198

Email: jorge.ripoll@uc3m.es

or

Jens V. Stein

Theodor Kocher Institute

University of Bern

Freiestr. 1

3012 Bern

Switzerland

Tel. + 41 31 631 5390

Fax + 41 31 631 3799

Email: jstein@tki.unibe.ch

Highlights

- Light sheet fluorescence microscopy enables single cell detection inside lymph nodes
- Lymph node-optimized clearing procedures preserve fluorescent protein signal
- Calibration protocols facilitate organ-wide interaction analysis of rare cells

Keywords

Light sheet fluorescence microscopy; tissue clearing; lymph nodes; T cell – DC interactions

Abstract

Reactive lymph nodes (LNs) are sites where pMHC-loaded dendritic cells (DCs) interact with rare cognate T cells, leading to their clonal expansion. While DC interactions with T cell subsets critically shape the ensuing immune response, surprisingly little is known on their spatial orchestration at physiologically T cell low precursor frequencies. Light sheet fluorescence microscopy and one of its implementations, selective plane illumination microscopy (SPIM), is a powerful method to obtain precise spatial information of entire organs of 0.5 – 10 mm diameter, the size range of murine LNs. Yet, its usefulness for immunological research has thus far not been comprehensively explored. Here, we have tested and defined protocols that preserve fluorescent protein function during lymphoid tissue clearing required for SPIM. Reconstructions of SPIM-generated 3D data sets revealed that calibrated numbers of adoptively transferred T cells and DCs are successfully detected at a single cell level within optically cleared murine LNs. Finally, we define parameters to quantify specific interactions between antigen-specific T cells and pMHC-bearing DCs in murine LNs. In sum, our studies describe the successful application of light sheet fluorescence microscopy to immunologically relevant tissues.

1. Introduction

During adaptive immune responses, reactive lymph nodes (LNs) serve as meeting points where antigen-specific T cells encounter and become activated by dendritic cells (DCs). Since activation of antigen-specific T cells requires the direct physical contact with pMHC-bearing DCs and only 1 in 10^5 - 10^6 T cells carries a cognate TCR, they continuously scan the surfaces of DCs before firm arrest (Bajénoff et al., 2007; Bousso, 2008; Mempel et al., 2004). Given the scarcity of cognate T cell – DC interactions at the onset of an immune response, the mode of interactions between T cell subsets that contribute to the full development of adaptive immunity has not yet been fully elucidated. As example, optimal $CD8^+$ T cell activation and memory formation depends on help delivered by initially rare cognate $CD4^+$ T cells. Various hypothesis have been developed to model $CD4^+$ help. $CD4^+$ T cell-mediated licensing of DCs was shown to play a role during $CD8^+$ T cell expansion (Bennett et al., 1998; Ridge et al., 1998; Schoenberger et al., 1998). Recent intravital twophoton microscopy (2PM; also referred to as multiphoton microscopy) of adoptively transferred T cells and DCs in murine LNs indeed identified specific DC subsets that may serve as sequential communication platform for $CD4^+$ and $CD8^+$ T cells (Eickhoff et al., 2015; Hor et al., 2015). On the other hand, 2PM studies have also uncovered simultaneous docking of cognate $CD8^+$ and $CD4^+$ T cells at the same DCs, leading to the proposal of chemoattractant gradients that mediate efficient interplay of $CD4^+$ and $CD8^+$ T cells (Castellino et al., 2006). However, a major caveat of 2PM studies is the requirement to transfer > 10^6 TCR transgenic T cells in order to observe sufficient events for a meaningful statistical analysis in the limited FOV of 2PM recordings. This leads to precursor frequencies that are several orders of magnitude above physiological levels of 1-20 cells/LN (Moon et al., 2007), and as a consequence, the occurrence of leukocyte interactions is likely to be vastly overestimated in such settings. Thus, the spatial relation between T cell subsets and DCs during early immune responses has remained elusive when using physiologically low numbers of cells.

Light sheet fluorescence microscopy (LSFM) and one of its implementations, selective plane illumination microscopy (SPIM), is based on the generation of a thin laser sheet oriented orthogonally to the detection axis, illuminating a single plane at the focal distance of the detection objective (Huisken et al., 2004; Reynaud et al., 2014). By moving the sample through the light sheet, a 3D image stack is quickly obtained for quantitative analysis. LFSM has thus far been mainly applied in developmental biology to study processes in naturally transparent organisms such as *Caenorhabditis elegans* or *Danio rerio*, and is suited for optical sectioning of whole biological organs at single cell resolution (Arranz et al., 2014; 2013; Ntziachristos, 2010). Furthermore, LSFM has the potential to become a method of choice for detection of immune cell subsets within their native environment. In fact, using tissue clearing with the organic compound BABB, we and others have used SPIM to identify lymphocytes and DCs inside lymphoid tissue (Brede et al., 2012; Coelho et al., 2013; Mayer et al., 2012). However, the potential of SPIM to identify rare leukocyte interactions in lymphoid tissue has thus far not been comprehensively analyzed. Furthermore, BABB treatment quenches fluorescent protein signals, which is a serious caveat when following dividing T cells, since BABB-resistant molecular dyes dilute with each cell division.

Based on recent advances in tissue clearing methods, which preserve fluorescent protein function, visualization of fluorescent protein-expressing cells has become possible even in deep parts of opaque tissues such as brain. Scale solutions are one of the first examples of tissue clearing methods that preserve the activity of fluorescent proteins by using aqueous clearing solution (Hama et al., 2011). However, Scale solutions cause tissue enlargement and require weeks to months for clearing. Therefore, alternative clearing protocols including ClearT2 (Kuwajima et al., 2013), SeeDB (Ke et al., 2013), 3DISCO (Ertürk et al., 2012), and CUBIC (Susaki et al., 2014) have been developed. Although all these methods have been reported to preserve fluorescent proteins in the brain, distinct organs respond to clearing solutions differently. Thus, clearing protocols have to be adapted to achieve sufficient clearing and preservation of fluorescent proteins at the same time. Here, we tested a

variety of recently published clearing protocols on mouse LNs, identifying an optimal fluorescent protein signal-preserving protocol. Furthermore, we developed a comprehensive protocol for SPIM imaging of entire LNs to calibrate numbers and positions of adoptively transferred T cells and DCs for interaction analysis of rare cells. Our proof-of principle experiments support the applicability of SPIM in uncovering mechanisms governing initial events during activation of physiologically low numbers of pMHC-specific T cells within LNs.

2. Materials and methods

2.1. Mice

C57BL/6 mice were purchased from Janvier (AD Horst). *Rag1*$^{-/-}$ OT-I CD8^{+} TCR tg mice recognizing $OVA_{257-264}$ in the context of MHC class I K^{b} (Hogquist et al., 1994) and OT-II CD4^{+} TCR tg mice recognizing $OVA_{323-339}$ in the context of MHC class II I-A^{b} (Barnden et al., 1998) were maintained in SPF conditions at the Department of Clinical Research Animal facility of the University of Bern. To generate bone marrow (BM) chimeric mice, C57BL/6-Tg(CAG-EGFP)131Osb/LeySopJ (Ubi-GFP) tg mice with ubiquitous GFP expression were given a single dose of 7.5 Gy irradiation and transplanted with 5 x 10^{6} total BM cells from C57BL/6 mice one day later. BM chimeric mice were rested for > 6 weeks before use. All animal work has been approved by the Cantonal Committee for Animal Experimentation and conducted according to federal guidelines.

2.2. T cell purification

Peripheral LNs and spleens from C57BL/6, *Rag1*$^{-/-}$ OT-I and OT-II mice were harvested and homogenized using a 70-µm cell strainer. Untouched total T cells and CD4^{+} T cells were isolated with EasySep Mouse negative selection kit according to the manufacturer`s protocol (StemCell Technologies). Cell purity was typically > 90%.

2.3. DC culture and peptide pulsing

DCs were *in vitro* differentiated from femur and tibia bone marrow of C57BL/6 mice as described (Moalli et al., 2014). During the final 24 h of culture, cell were stimulated with LPS (1 µg/ml; Sigma Aldrich) and left unpulsed or were pulsed with 100 nM $OVA_{257-264}$ (SIINFEKL) and 10 µM $OVA_{323-339}$ (ISQAVHAAHAEINEAGR) peptides (45 min, 37^{o}C).

2.4. Cell labelling and adoptive transfer

Purified $CD8^+$ and $CD4^+$ T cells as well as peptide-pulsed DCs (1 x 10^7 cells/ml) were labelled with fluorescent dyes (all from Invitrogen) 5-chloromethylfluorescein diacetate (CMFDA; CellTracker Green; 3 µM, 15 min); 4,4-difluoro-4-bora-3a,4a-diaza-*s*-indacene (BODIPY 630/650; 5 µM, 20 min); 5-(and-6)-(((4-chloromethyl)benyoyl)amino tetramethylorhodamine (CMTMR; CellTracker Orange; 5 µM, 30 min). In some cases, we used GFP-expressing OT-I T cells for adoptive transfer. Fluorescently labelled T cells were i.v. injected as indicated, while DCs were s.c. injected into hind footpad of recipient sex-matched C57BL/6 mice.

2.5. Clearing protocols for murine LNs

Where indicated, BM chimera mice received s.c. footpad injections of Alexa Fluor 594-coupled anti-Lyve1 (2 µg/mouse; Clone 223322, R&D systems) one day before isolation of popliteal LNs to label the lymphatic network. Twenty minutes before LN harvest, WT and BM chimera mice received i.v. Alexa Fluor 633-conjugated MECA-79 mAb (5 µg/mouse; Nanotools, Freiburg, Germany) to label high endothelial venules (HEVs). Coupling of Abs to Alexa dyes were performed according to the manufacturer's instructions (Molecular Probes). Isolated LNs were fixed with 0.4% paraformaldehyde solution (24 h, 4°C), followed by careful removal of surrounding fat tissue under a stereomicroscope. For clearing in BABB (1 : 2 v/v Benzylalcohol : Benyzlbenzoate; Sigma), LNs were embedded in 1.3% low melting point agarose (Invitrogen, Eugene, OR), dehydrated in 100% methanol and optically cleared in BABB as described (Mayer et al., 2012). For 3DISCO, LNs were fixed in 4% paraformaldehyde, dehydrated in tetrahydrofuran series, and cleared with dibenzyl ether without embedding in agarose as described (Ertürk et al., 2012). Alternatively, isolated LNs were fixed with 4% paraformaldehyde solution (24 h, 4°C) and embedded in 2% low melting point agarose before or after addition of various clearing solutions. For SeeDB, LNs were embedded in agarose and treated as described (Ke et al., 2013). For ClearT2, LNs were treated as described (Kuwajima et al., 2013), followed by agarose embedding and further incubation with ClearT2 solution. For CUBIC, fixed LNs were treated

with CUBIC reagent 1 for 2-3 days as described (Susaki et al., 2014). For large LNs, CUBIC reagent 1 was replaced every 24 h. Then, LNs were embedded in 2% low melting point agarose followed by sequential dehydration in 30% sucrose (1 day, 4^{o}C) and 50% sucrose (2 days, 4^{o}C). Dehydrated LNs were optically cleared in CUBIC reagent 2 (1 day, room temperature).

2.6. Selective plane illumination microscopy (SPIM)

Imaging was performed on a self-built light sheet microscope based on a previously published SPIM setup (Mayer et al., 2012). In some cases, we also used the original SPIM device for image acquisition. The light sheet microscope is equipped with five lasers (20 mW 405 nm/MDL-III, Roithner; 100 mW 487 nm/iBEAM-SMART-488-S, Toptica; 30 mW 561 nm/MGL-FN, Roithner; 20 mW 593.5 nm/MGL-III, Roithner; 50 mW 635 nm/MRL-III, Roithner) and six bandpass filters (447/60, 490/40, 525/50, 593/46, 628/40, and 670/30), which can be freely combined to use optimal setting for each fluorophore. A light sheet was formed using a cylindrical lens (Melles Girot) and an N-PLAN 2.5x/0.07 POL objective (Leica). Three micro-translation stages (M-112.1DG, Physik Instrumente) and one precision rotary stage (M-116.DGH, Physik Instrumente) compose the sample stage controlled via motor controllers (C-863.11 Mercury, Physik Instrumente) assigned to each axis of the stage. Samples were kept in a quartz cuvette (20 mm x 20 mm x 35 mm, 2 mm in thickness) filled with clearing solution during imaging. Images were recorded using an N-PLAN EPI 5x/0.12 and a digital CCD camera (Orca-R^2 C10600, Hamamatsu). The SPIM was controlled by customized software for automated hardware control of multispectral image acquisition (4D-Nature, Madrid, Spain).

2.7. Image analysis and quantification

Acquired 3D data stacks were reconstructed with Volocity (Perkin Elmer) or Imaris (Bitplane) software. After introducing the correct XYZ image properties, images were processed for noise removal and for detection of cells within reconstructed datasets. Cells

were identified as objects based on the intensity of fluorescence in the respective channel and filtered based on the size, and level of the background fluorescence in other channels. Volocity was used to calculate minimum distances between T cell centroids and the centroid position of the nearest neighbor DC. Imaris isosurface algorithm was used to identify LN surface and volume from the autofluorescent channel.

2.8. Statistical analysis

Data were analyzed in Prism 6 (GraphPad) using Mann-Whitney or Kruskal-Wallis tests. P values < 0.05 were considered significant.

3. Results

3.1. Customized SPIM setup for LN imaging

We adapted a published SPIM setup (Mayer et al., 2012) specifically for mouse LN imaging with multiple excitation and detection channels for the identification of transferred cell populations and anatomical landmarks. We combined 5 laser lines (405 nm, 488 nm, 561 nm, 593 nm, 633 nm) and corresponding detection filters (447/60, 490/40, 525/50, 593/46, 628/40, and 670/30) and projected the laser sheets onto cleared samples in a 2 cm x 2 cm cuvette, which is optimized for organs up to 5 mm (**Figures 1A and 1B**). Agarose-embedded samples were held in place by gluing to a custom-made holder, which prevented unwanted slipping of the sample during translocation (**Figure 1C**). Since one of our aims was to assess the spatial relationship between transferred cells labelled with different fluorophores or expressing fluorescent proteins, we calibrated the laser sheets such that all laser lines showed perfect overlap. The half-maximum full distance beam widths were 8-12 µm for all lasers (not shown). The SPIM setup was controlled by customized software developed to control the motors, lasers and camera of the SPIM setup (**Figure 1D**). A typical image acquisition procedure involved the LED white-light guided positioning of the LNs in the center of the CCD Camera FOV to set the origin of scan field and, when needed, lateral (x, y) scanning area. To determine the axial scanning range, we used 405 nm excitation with 447/60 emission filter to find the axial end of the sample. The exposure time was determined for each set of excitation/emission pair to produce an optimal signal-to-noise ratio without saturating the signal. Following image acquisition with z-spacing of 5 – 10 µm yielding typically 200 – 300 images per channel, we transferred the stacks for analysis in commonly used image analysis software.

3.2. Comparison of clearing methods for murine LNs

Many biological samples make use of fluorescent proteins (FPs), which allows long-term detection of adoptively transferred cells or the identification of stromal structures. In order to

apply quantitative tissue-wide SPIM imaging without restriction of dye lifetime, we performed a comprehensive analysis of various published clearing methods that reportedly preserve FP fluorescence (**Table 1**). Given its efficient tissue clearing capability, we first tested an organic solvent based protocol, 3DISCO, which had been reported to preserve FP signal in neuronal mouse tissues (Ertürk et al., 2012). With LNs, however, we observed noticeable bleaching of GFP fluorescence during dehydration with tetrahydrofuran (**Figure 2A**). The bleaching manifested more after optical clearing with dibenzyl ether, which prevented its use for LN clearing (**Figure 2B**).

We therefore tested milder optical clearing protocols that are based on aqueous solutions. We chose ClearT2, SeeDB, and CUBIC as candidates. All three had been reported to preserve FPs while efficiently clearing the brain and minimizing tissue shrinkage (Ke et al., 2013; Kuwajima et al., 2013; Susaki et al., 2014). Neither SeeDB nor ClearT2, however, sufficiently cleared agarose-embedded LNs (**Table 1**). Furthermore, the ClearT2 formulation deformed agarose gels, precluding its use with agarose-embedded LNs (not shown). In contrast, a LN-adapted CUBIC protocol using agarose embedding and customized dehydration steps preserved GFP signal in LNs isolated from BM chimeric mice expressing GFP in radioresistant cells (**Figures 2C – E**). Thus, the CUBIC protocol is suitable for the analysis of LNs containing FP-expressing cells.

To gauge the clearing efficacy of CUBIC for LNs, we compared LNs isolated from the same donor mouse after optical clearing by either CUBIC or the “gold standard” BABB. We stained LNs *in vivo* with Alexa Fluor-conjugated anti-Lyve-1 and anti-PNAd to label lymphatic vessels and HEVs as landmarks, respectively (**Figures 2C and 2D**). We found that while both BABB and CUBIC treatment allowed to detect lymphatic and high endothelial vessels, there were some differences. Overall, BABB clearing yielded slightly smaller LNs owing to dehydration, whereas CUBIC-cleared LNs were mildly enlarged (**Figure 2C**). BABB-cleared LNs had lost parenchymal GFP signal in the corresponding channel other than autofluorescent signals from the LN capsule, but showed a slightly improved clearing efficacy for molecular dyes (**Figures 2D and 2E**).

Adoptive transfer experiments are commonly used in immunology to study T cell immune responses to infectious agents or model antigens presented by DCs. Such experiments are based on i.v. injection of congenically or fluorescently labeled T cells isolated from a donor to a recipient mouse. We therefore analyzed whether rare GFP-expressing T cells could be identified after adoptive transfer and CUBIC clearing. We transferred 1 x 10^4 GFP^+ OT-I T cells into mice followed by s.c. transfer of cognate peptide pulsed DCs. Two days later, draining LNs were isolated and cleared with CUBIC. We were able to detect individual T cells in close contact with DCs in the T cell area (**Figures 3A and B**). Taken together, CUBIC clearing is ideally suited for LN clearing in situations where FP fluorescence needs to be preserved.

3.3. T cell transfer calibration

We examined whether gradually decreasing adoptively transferred T cell numbers could be reliably retrieved from whole-mount SPIM images. To maximize the image quality, we performed these experiments using BABB-cleared LNs. We i.v. transferred 1 x 10^3, 1 x 10^4 and 1 x 10^5 CMTMR-labeled T cells and isolated popliteal LNs 24 later. In recipient mice, we also labeled the HEV network as described in Materials and Methods. SPIM reconstruction allowed us to precisely identify transferred T cells within lymphoid tissue (**Figure 4A**). In popliteal LNs of mice that had received 1 x 10^5 T cells, we recovered 365 ± 44 cells (mean ± SD, n = 4). The corresponding numbers for LNs from 1 x 10^4 T cells recipients was 32 ± 8 (n = 3). Remarkably, we were able to identify between 2 – 7 T cells in LNs of mice that had received 1 x 10^3 T cells systemically (**Figure 4B**), whereas no T cells were detected without T cell transfer (not shown). The average percentage of T cells recovered from one popliteal LN over total transferred T cells remained stable (0.47 ± 0.25%, 0.32 ± 0.08 and 0.36 ± 0.04%; mean ± SD; for 1 x 10^3, 1 x 10^4 and 1 x 10^5 i.v. transferred T cells, respectively) (**Figure 4C**). We also calculated the distribution of adoptively transferred T cells relative to the HEV network from the samples that had received 1 x 10^5 T cells (**Figure 4D**). One day post transfer, we found that 3.3 ± 1.9% of

transferred T cells were intravascular, while 7.2 ± 2.5% were perivascular and 89.4 ± 3.9% in the LN parenchyme, which suggests equilibrium of the transferred population (**Figure 4E**). As predicted, the T cell transfer had no influence on the overall LN volume (**Figure 4F**).

3.4. DC transfer calibration

We titrated the number of LPS-matured, fluorescently labeled DCs that arrive in draining LNs after s.c. injection into the hind footpad (1 x 10^4, 1 x 10^5, 1 x 10^6 in 10 µl). After 24 h, we isolated the HEV-labeled popliteal LNs of recipient mice and performed SPIM imaging (**Figure 5A**). While numbers of recovered DCs varied slightly more than for T cells, we identified in average 10680 ± 7063 DCs in LNs draining footpads with 1 x 10^6 DCs (n = 4). This number decreased to 533 ± 415 and 29 ± 19 DCs in LNs of mice that had received 1 x 10^5 and 1 x 10^4 DCs, respectively (**Figure 5B**). When normalized to the input, we observed a non-significant trend for a rise in DC recovery with increasing DC dose (0.29 ± 0.19%, 0.53 ± 0.41% and 1.07 ± 0.71% for 1 x 10^4, 1 x 10^5 and 1 x 10^6 s.c. injected DCs, respectively; **Figure 5C**), which presumably reflects cooperativity in DCs migration through tissue conditioning. Our DC recovery rate in draining LNs when s.c. injecting 1 x 10^6 DCs or more is consistent with a previous report (Celli et al., 2012). In addition, we observed a gradual increase in LN size with increasing DC injections, which reached statistical significance in recipients of 1 x 10^6 DCs (**Figure 5D**). In enlarged LNs, we could also detect the accumulation of DCs in the subcapsular and interfollicular regions (**Figure 5A**), as described (Mayer et al., 2012). In sum, our calibration studies with adoptively transferred leukocytes confirmed the suitability of SPIM reconstructions to reliably detect low numbers of cells in large tissue volumes.

3.5. Analysis of T cell – DC interactions using SPIM

Based on our titration experiments, we explored under which conditions SPIM-based whole-organ imaging is suitable for the identification of antigen-driven T cell – DC

interactions. We transferred LPS-matured, fluorescently labeled DCs, which were either left unpulsed or were pulsed with $OVA_{257-264}$ and $OVA_{323-339}$ peptides, into hind footpads of recipient mice at a low (2 x 10^4 of each) and high concentration (2 x 10^5 of each). Purified OT-I and OT-II T cells (5 x 10^4 of each) were i.v. injected 18 h later and allowed to accumulate in draining LNs for another 8 h (**Figure 6A**). When we analyzed LNs that contained low numbers of DCs, we identified close proximity of OT-I and OT-II T cells with pulsed DCs (**Figure 6B**), suggesting specific interactions. Furthermore, we detected occasional "triplet" interactions, with OT-I and OT-II T cells binding jointly to the same DC (not shown). We performed an automated distance measurement of T cell and DC centroid positions, which was followed by a visual inspection of all measured distances. With the optical and experimental settings used, we found that the vast majority of T cell – DC centroid distances of less than 20 µm were confirmed by visual inspection to be in close proximity. In turn, most centroid positions of more than 20 µm distance were found to be non-interacting by visual inspection (**Figure 6C**). Thus, we defined 20 µm as a cutoff T cell – DC centroid distance to define cognate T cell – DC interactions under conditions where DCs were sparse in LN tissue. This finding was corroborated when we compared T cell – DC centroid distances in LNs containing low numbers of unpulsed DCs. Under these conditions, only few OT-I or OT-II centroid positions were closer than 20 µm to the centroid positions of unpulsed DCs (**Figures 6D and 6E**). In contrast, when examining LNs containing high numbers of DCs, T cell centroid positions determined by SPIM imaging were found similarly close to both unpulsed and pulsed DCs when the 20 µm distance cutoff was applied (**Figures 6D and 6E**). Thus, SPIM is particularly effective in identifying specific T cell – DC interactions when DC numbers are low, whereas higher DC numbers lead to comparable centroid position proximities irrespective of pMHC presentation.

4. Discussion

LSFM is a powerful method to obtain precise spatial information on cell distribution within entire organs, yet its usefulness for immunological research had not been comprehensively explored. Here, we have tested and defined protocols and parameters that allow one of its implementations, SPIM, to uncover rare interactions of TCR tg T cells and pMHC-bearing DCs. Reconstruction of SPIM-generated 3D data sets revealed that low numbers of adoptively transferred T cells are successfully detected within optically cleared popliteal LNs that are approximately 0.5 – 1.5 mm^3 in volume. Taken together, our studies identify parameters for successful application of LSFM to immunologically relevant tissues.

Although optical clearing with organic solvents like BABB support efficient LN clearing (Brede et al., 2012; Coelho et al., 2013; Mayer et al., 2012), FPs typically become quenched by BABB. Our analysis of recently published clearing methods has uncovered CUBIC as the currently optimal approach to identify rapidly dividing FP-expressing T cells (Figure 3 and not shown). Another method called CLARITY uses electric current to promote active tissue clearing (Chung and Deisseroth, 2013). While we have not explored this approach for LNs, the ease of use of CUBIC makes this the method of choice for preserving fluorescent protein function when required. CUBIC clearing is not limited to adoptive transfer experiments, since it also enables visualization of endogenous, fluorescently tagged immune cell subsets. In this regard, SPIM might become useful to define the localization of fluorescently labeled endogenous DCs subsets, infected cells, or IL-2, IFN-γ or TNF-α producing activated T cells. Additionally, CUBIC clearing is compatible with fixed whole mount tissue staining in PBS, either before or after CUBIC1 solution (not shown), similar to B cell follicle staining protocols used for OPT sample preparations (Kumar et al., 2010).

In our experiments, we have focused on popliteal LNs, since these are well suited for controlled DC transfer via footpad injection and amenable for twophoton experiments, which serve to complement fixed whole organ imaging with dynamic leukocyte migration

and interaction data. We have also successfully applied our CUBIC clearing protocol to larger inguinal LNs, indicating that it should be applicable to all LNs, while spleen becomes only partially cleared after prolonged incubation *ex vivo* (not shown). A recent refinement of CUBIC clearing based on direct perfusion of CUBIC1 solution into mice reportedly clears entire spleens efficiently (Susaki et al., 2015). We have confirmed the suitability of the CUBIC perfusion protocol for clearing of large salivary glands (not shown).

Our adoptive transfer data identified labeled T cells at a single cell level and provided precise information on their microenvironmental distribution using HEVs as anatomical landmarks. Furthermore, we uncovered a linear relationship between number of injected and detected T cells. These results allow us to reassess the actual "take" of adoptively transferred T cells (i.e. stably recirculating population), which is widely assumed to be 10% of the injected cells based on flow cytometry data. Assuming that popliteal LNs contain approximately 2 x 10^6 lymphocytes, i.e. 1% of the total lymphocyte population of 2 x 10^8 cells (Moon et al., 2007), we estimate that at least 35-40% of transferred T cells actually engraft in recipient mice with the low numbers of transferred cells used here. This difference to flow cytometric data most likely arises from the low cell recovery when preparing single cell suspensions for flow cytometry by mechanical disruption or enzymatic digestion, as recently documented for tissue-resident T cells (Steinert et al., 2015). This may be further confounded by the reported difficulty to extract T cells interacting with DCs (Maxwell et al., 2004).

When low numbers of DCs were transferred, the frequency of close cellular contacts with T cells was significantly increased by the presence of cognate pMHCs, suggesting an antigen-driven nature of these interactions. Strikingly, the presence of low amounts of DCs loaded with cognate pMHCs exerted a global effect on the overall distribution of OT-I and OT-II T cells in LNs. On average, the minimal distance of analyzed OT-I and OT-II T cells to pulsed DCs was smaller as compared to unpulsed DCs, even without direct contact (i.e. > 20 µm centroid distances). This suggests that at the time point analyzed (8 h post transfer), antigen-specific T cells were still actively sampling in close proximity to DCs for signal

integration while others may have engaged in stable interactions. This antigen-driven population-wide shift towards DCs is reminiscent of T cell swarming around DC clusters described in 2PM experiments (Miller et al., 2004), and may reflect chemoattractant influence on T cell motility (Castellino and Germain, 2006; Hugues et al., 2007). In any event, our data suggest that minimum distance between two cell subsets serve as a reliable surrogate read-out of real interactions when low numbers of DCs are present in LNs. At high DC density, our automated centroid distance analysis found T cells to be in close proximity to DCs irrespective of pMHC presentation, highlighting the limits of SPIM-based interaction analysis. From a physiological perspective, low abundance of cognate pMHC-presenting DCs presumably corresponds to early time points during a course of infection when only rare DCs present pathogen-derived peptides. Over time, incoming DCs or spreading infection will lead to a rise in the amount of cells presenting cognate pMHC, suggesting that the importance of active T cell scanning might be less critical at later stages of the immune response. However, this has thus far not been experimentally addressed.

Mesoscopic imaging techniques, i.e. those that are able to image organs or embryos between 0.5 – 10 mm in size, have been previously applied to LN imaging. We have used Optical Projection Tomography (OPT) to catalog the 3D HEV network and B cell follicle distribution in resting and inflamed LNs (Coelho et al., 2013; Kumar et al., 2010; 2012). Because of the required depth of focus for OPT reconstructions (Sharpe et al., 2002), the numerical aperture of most OPT devices is limited and single cell resolution is not supported. On the other hand, we found that quantification of anatomical landmarks such as HEVs is actually simpler in OPT than in SPIM reconstructions, because OPT reconstructions are isotropic and more amenable for reconstruction of filamentous structures used for vascular analysis (Kumar et al., 2012). An alternative approach to SPIM for identification of single cells called For3D has been recently published and consists of an automated 3D reconstruction of mouse lymphoid organ sections imaged by confocal microscopy (Irla et al., 2013). The advantage of For3D is that immunofluorescent labeling is performed on sections, thus bypassing potential shortcomings of whole-organ staining

procedures. Furthermore, this approach produces high resolution images owing to the recording of sections by confocal microscopy. As a drawback, For3D is time-consuming since it requires physical sectioning of the specimen and potentially error-prone 3D reassembly of sections. The advantage of the SPIM platform we present here is the speed of image acquisition, at the expense of high resolution. Thus, we routinely scan 4-8 cleared LNs per day containing various fluorescent cell populations. A limitation of our SPIM setup is that fine structures such as DC dendrites are not resolved, owing to the low magnification and NA. This makes it difficult to assess whether direct contacts between T cells and DC do take place, in particular at high DC densities. When increasing the magnification to 20X, we were able to detect single DC dendrites, although it remained unclear whether all dendrites could be identified. Similarly, when analyzing high resolution confocal LN sections, we noticed that many fine (0.5 – 1 µm thickness) connections between stromal cells of the T cell area were not detected even in 20X SPIM LN reconstructions (not shown). Furthermore, the reduced FOV at high magnifications required stitching of multiple scans to obtain a complete LN overview. We therefore propose that SPIM is particularly useful for an unbiased analysis of leukocyte distribution and cellular interactions within entire LNs at physiologically relevant low cell numbers. This could be in the future exploited to critically address the role of direct versus indirect $CD4^+$ T cell help on developing $CD8^+$ T cell responses (Castellino and Germain, 2006; Eickhoff et al., 2015; Hor et al., 2015). In particular, the notion that chemokines specifically attract T cell subsets to form multicellular complexes can now be directly addressed with low precursor frequencies, thus bypassing potential artifacts introduced by transfer of large precursor numbers. Similarly, simultaneous versus subsequent docking of $CD4^+$ and $CD8^+$ T cells at specific DC subsets is now realistically achievable, given the relatively high throughput of SPIM-based LN 3D imaging. Since SPIM reconstructions only provide a snapshot of a fixed LN, these experiments need to be carefully controlled and accompanied by an unbiased modelling approach (Ludewig et al., 2012).

In sum, our results confirm that SPIM analysis is suitable to address cellular distribution within LNs with regard to other immune cell subsets or anatomical landmarks at physiologically relevant precursor frequencies. In combination with molecular probes that reflect the activation status of transferred cells, this method might permit a functional analysis of unfolding immune responses on an organ-wide level.

Authors contribution

JA, AO and JSw performed experiments. JR developed the SPIM control software and built the SPIM setup in Bern with help from JSw and JSh. JVS supervised the project, and all coauthors contributed to the final manuscript.

Acknowledgments

This work was funded by Swiss National Foundation grant 31003A_135649 (to JVS), Sinergia grant CR23I3_156234 and CRSII3_141918 (to JSh and JVS), EC FP7 Marie Curie RG grant 276702 (to JVS), and a Novartis Research grant (to AO). JA was supported by Postdoctoral Fellowship for Research Abroad from Japan Society for the Promotion of Science. JR acknowledges support from the EC FP7 CIG grant HIGH-THROUGHPUT TOMO, and MINECO grant FIS2013-41802-R MESO-IMAGING. JSw and JSh acknowledge support of the Spanish Ministry of Economy and Competitiveness, 'Centro de Excelencia Severo Ochoa 2013-2017', SEV-2012-0208. The SPIM setup was financed by a grant of the Pierre Mercier Foundation.

References

Arranz, A., Di Dong, Zhu, S., Savakis, C., Tian, J., Ripoll, J., 2014. In-vivo Optical Tomography of Small Scattering Specimens: time-lapse 3D imaging of the head eversion process in Drosophila melanogaster. Sci Rep 4, 7325. doi:10.1038/srep07325

Arranz, A., Dong, D., Zhu, S., Rudin, M., Tsatsanis, C., Tian, J., Ripoll, J., 2013. Helical optical projection tomography. Opt Express 21, 25912–25925. doi:10.1364/OE.21.025912

Bajénoff, M., Egen, J.G., Qi, H., Huang, A.Y.C., Castellino, F., Germain, R.N., 2007. Highways, byways and breadcrumbs: directing lymphocyte traffic in the lymph node. Trends Immunol 28, 346–352. doi:10.1016/j.it.2007.06.005

Barnden, M.J., Allison, J., Heath, W.R., Carbone, F.R., 1998. Defective TCR expression in transgenic mice constructed using cDNA-based alpha- and beta-chain genes under the control of heterologous regulatory elements. Immunol Cell Biol 76, 34–40. doi:10.1046/j.1440-1711.1998.00709.x

Bennett, S.R.M., Carbone, F.R., Karamalis, F., Flavell, R.A., Miller, J.F.A.P., Heath, W.R., 1998. Help for cytotoxic-T-cell responses is mediated by CD40 signalling. Nature 393, 478–480. doi:10.1038/30996

Bousso, P., 2008. T-cell activation by dendritic cells in the lymph node: lessons from the movies. Nat Rev Immunol 8, 675–684. doi:10.1038/nri2379

Brede, C., Friedrich, M., Jordán-Garrote, A.-L., Riedel, S.S., Bäuerlein, C.A., Heinze, K.G., Bopp, T., Schulz, S., Mottok, A., Kiesel, C., Mattenheimer, K., Ritz, M., Krosigk, von, V., Rosenwald, A., Einsele, H., Negrin, R.S., Harms, G.S., Beilhack, A., 2012. Mapping immune processes in intact tissues at cellular resolution. J Clin Invest 122, 4439–4446. doi:10.1172/JCI65100

Castellino, F., Germain, R.N., 2006. Cooperation between CD4+ and CD8+ T cells: when, where, and how. Annu Rev Immunol 24, 519–540. doi:10.1146/annurev.immunol.23.021704.115825

Castellino, F., Huang, A.Y., Altan-Bonnet, G., Stoll, S., Scheinecker, C., Germain, R.N., 2006. Chemokines enhance immunity by guiding naive CD8+ T cells to sites of CD4+ T cell-dendritic cell interaction. Nature 440, 890–895. doi:10.1038/nature04651

Celli, S., Day, M., Müller, A.J., Molina-Paris, C., Lythe, G., Bousso, P., 2012. How many dendritic cells are required to initiate a T cell response? Blood. doi:10.1182/blood-2012-01-408260

Chung, K., Deisseroth, K., 2013. CLARITY for mapping the nervous system. Nat Meth 10, 508–513. doi:doi:10.1038/nmeth.2481

Coelho, F.M., Natale, D., Soriano, S.F., Hons, M., Swoger, J., Mayer, J., Danuser, R., Scandella, E., Pieczyk, M., Zerwes, H.-G., Junt, T., Sailer, A.W., Ludewig, B., Sharpe, J., Figge, M.T., Stein, J.V., 2013. Naive B-cell trafficking is shaped by local chemokine availability and LFA-1-independent stromal interactions. Blood 121, 4101–4109. doi:10.1182/blood-2012-10-465336

Eickhoff, S., Brewitz, A., Gerner, M.Y., Klauschen, F., Komander, K., Hemmi, H., Garbi, N., Kaisho, T., Germain, R.N., Kastenmuller, W., 2015. Robust Anti-viral Immunity Requires Multiple Distinct T Cell-Dendritic Cell Interactions. Cell. doi:10.1016/j.cell.2015.08.004

Ertürk, A., Becker, K., Jährling, N., Mauch, C.P., Hojer, C.D., Egen, J.G., Hellal, F., Bradke, F., Sheng, M., Dodt, H.-U., 2012. Three-dimensional imaging of solvent-cleared organs using 3DISCO. Nat Protoc 7, 1983–1995. doi:10.1038/nprot.2012.119

Hama, H., Kurokawa, H., Kawano, H., Ando, R., Shimogori, T., Noda, H., Fukami, K.,

Sakaue-Sawano, A., Miyawaki, A., 2011. Scale: a chemical approach for fluorescence imaging and reconstruction of transparent mouse brain. Nature Neuroscience 14, 1481–1488. doi:10.1038/nn.2928

Hogquist, K.A., Jameson, S.C., Heath, W.R., Howard, J.L., Bevan, M.J., Carbone, F.R., 1994. T cell receptor antagonist peptides induce positive selection. Cell 76, 17–27. doi:10.1016/0092-8674(94)90169-4

Hor, J.L., Whitney, P.G., Zaid, A., Brooks, A.G., Heath, W.R., Mueller, S.N., 2015. Spatiotemporally Distinct Interactions with Dendritic Cell Subsets Facilitates CD4(+) and CD8(+) T Cell Activation to Localized Viral Infection. Immunity. doi:10.1016/j.immuni.2015.07.020

Hugues, S., Scholer, A., Boissonnas, A., Nussbaum, A., Combadière, C., Amigorena, S., Fetler, L., 2007. Dynamic imaging of chemokine-dependent CD8+ T cell help for CD8+ T cell responses. Nat Immunol 8, 921–930. doi:10.1038/ni1495

Huisken, J., Swoger, J., Del Bene, F., Wittbrodt, J., Stelzer, E.H.K., 2004. Optical sectioning deep inside live embryos by selective plane illumination microscopy. Science 305, 1007–1009. doi:10.1126/science.1100035

Irla, M., Guenot, J., Sealy, G., Reith, W., Imhof, B.A., Sergé, A., 2013. Three-dimensional visualization of the mouse thymus organization in health and immunodeficiency. The Journal of Immunology 190, 586–596. doi:10.4049/jimmunol.1200119

Ke, M.-T., Fujimoto, S., Imai, T., 2013. SeeDB: a simple and morphology-preserving optical clearing agent for neuronal circuit reconstruction. Nature Neuroscience 16, 1154–1161. doi:10.1038/nn.3447

Kumar, V., Chyou, S., Stein, J.V., Lu, T.T., 2012. Optical projection tomography reveals dynamics of HEV growth after immunization with protein plus CFA and features shared with HEVs in acute autoinflammatory lymphadenopathy. Front. Immun. 3, 282. doi:10.3389/fimmu.2012.00282

Kumar, V., Scandella, E., Danuser, R., Onder, L., Nitschké, M., Fukui, Y., Halin, C., Ludewig, B., Stein, J.V., 2010. Global lymphoid tissue remodeling during a viral infection is orchestrated by a B cell-lymphotoxin-dependent pathway. Blood 115, 4725–4733. doi:10.1182/blood-2009-10-250118

Kuwajima, T., Sitko, A.A., Bhansali, P., Jurgens, C., Guido, W., Mason, C., 2013. ClearT: a detergent- and solvent-free clearing method for neuronal and non-neuronal tissue. Development 140, 1364–1368. doi:10.1242/dev.091844

Ludewig, B., Stein, J.V., Sharpe, J., Cervantes-Barragan, L., Thiel, V., Bocharov, G., 2012. A global "imaging‘’ view on systems approaches in immunology. 42, 3116–3125. doi:10.1002/eji.201242508

Maxwell, J.R., Rossi, R.J., McSorley, S.J., Vella, A.T., 2004. T cell clonal conditioning: a phase occurring early after antigen presentation but before clonal expansion is impacted by Toll-like receptor stimulation. J Immunol 172, 248–259. doi:10.4049/jimmunol.172.1.248

Mayer, J., Swoger, J., Ozga, A.J., Stein, J.V., Sharpe, J., 2012. Quantitative Measurements in 3-Dimensional Datasets of Mouse Lymph Nodes Resolve Organ-Wide Functional Dependencies. Computational and Mathematical Methods in Medicine 2012, 1–8. doi:10.1155/2012/128431

Mempel, T.R., Scimone, M.L., Mora, J.R., Andrian, Von, U.H., 2004. In vivo imaging of leukocyte trafficking in blood vessels and tissues. Curr Opin Immunol 16, 406–417. doi:10.1016/j.coi.2004.05.018

Miller, M.J., Safrina, O., Parker, I., Cahalan, M.D., 2004. Imaging the single cell dynamics of CD4+ T cell activation by dendritic cells in lymph nodes. J Exp Med 200, 847–856.

doi:10.1084/jem.20041236

Moalli, F., Cupovic, J., Thelen, F., Halbherr, P., Fukui, Y., Narumiya, S., Ludewig, B., Stein, J.V., 2014. Thromboxane A2 acts as tonic immunoregulator by preferential disruption of low-avidity CD4+ T cell-dendritic cell interactions. Journal of Experimental Medicine 211, 2507–2517. doi:10.1084/jem.20140137

Moon, J.J., Chu, H.H., Pepper, M., McSorley, S.J., Jameson, S.C., Kedl, R.M., Jenkins, M.K., 2007. Naive CD4(+) T cell frequency varies for different epitopes and predicts repertoire diversity and response magnitude. Immunity 27, 203–213. doi:10.1016/j.immuni.2007.07.007

Ntziachristos, V., 2010. Going deeper than microscopy: the optical imaging frontier in biology. Nat Meth 7, 603–614. doi:10.1038/nmeth.1483

Reynaud, E.G., Peychl, J., Huisken, J., Tomancak, P., 2014. Guide to light-sheet microscopy for adventurous biologists. Nat Meth 12, 30–34. doi:10.1038/nmeth.3222

Ridge, J.P., Di Rosa, F., Matzinger, P., 1998. A conditioned dendritic cell can be a temporal bridge between a CD4: +: T-helper and a T-killer cell : Article : Nature. Nature 393, 474–478. doi:10.1038/30989

Schoenberger, S.P., Toes, R.E., van der Voort, E.I., Offringa, R., Melief, C.J., 1998. T-cell help for cytotoxic T lymphocytes is mediated by CD40-CD40L interactions. Nature 393, 480–483. doi:10.1038/31002

Sharpe, J., Ahlgren, U., Perry, P., Hill, B., Ross, A., Hecksher-Sørensen, J., Baldock, R., Davidson, D., 2002. Optical projection tomography as a tool for 3D microscopy and gene expression studies. Science 296, 541–545. doi:10.1126/science.1068206

Steinert, E.M., Schenkel, J.M., Fraser, K.A., Beura, L.K., Manlove, L.S., Igyártó, B.Z., Southern, P.J., Masopust, D., 2015. Quantifying Memory CD8 T Cells Reveals Regionalization of Immunosurveillance. Cell 161, 737–749. doi:10.1016/j.cell.2015.03.031

Susaki, E.A., Tainaka, K., Perrin, D., Kishino, F., Tawara, T., Watanabe, T.M., Yokoyama, C., Onoe, H., Eguchi, M., Yamaguchi, S., Abe, T., Kiyonari, H., Shimizu, Y., Miyawaki, A., Yokota, H., Ueda, H.R., 2014. Whole-Brain Imaging with Single-Cell Resolution Using Chemical Cocktails and Computational Analysis. Cell 1–14. doi:10.1016/j.cell.2014.03.042

Susaki, E.A., Tainaka, K., Perrin, D., Yukinaga, H., Kuno, A., Ueda, H.R., 2015. Advanced CUBIC protocols for whole-brain and whole-body clearing and imaging. Nat Protoc 10, 1709–1727. doi:10.1038/nprot.2015.085

Figure legends

Figure 1. Selective plane illumination microscope (SPIM) of murine LNs. Schematic overview of the SPIM setup (A) and close-up of the imaging chamber (B). (C) Example of an agarose block containing a cleared murine LN (white arrowhead) glued to a customized metal holder (top) and immersed in the cuvette (bottom). (D) Screenshots of the customized software. An image of the current position appears in the snapshot window (1) with the selected excitation/emission (2) and exposure time (3). The settings in (2) and (3) are stored in a separate window (4) for whole-organ scanning. Sample position is controlled by the software with a stage controlling function (5). Scanning volume is set by defining initial and end point in x, y, and z axis (6). Throughout the process, the live view is displayed in a separate window (7). After setting up excitation/emission combinations and scanning volume, the step size of the scan are is set for each axis in the wizard (8). During the scan, current position, image, channel, and estimated time for scanning are displayed in a separate window (9).

Figure 2. Comparison of fluorescent protein signal preservation by different clearing methods. (A and B) Images of GFP signal loss in the course of LN clearing by 3DISCO. LNs from Ubi-GFP mice were dehydrated using increasing tetrahydrofuran series (20 min each), followed by an 18 h incubation for the third 100% incubation (A). After dehydration, LNs were cleared by incubating in dibenzyl ether for indicated times (B). GFP signal became substantially attenuated after incubation in dibenzyl ether. (C) SPIM-based images of LNs isolated from C57BL/6 -> Ubi-GFP BM chimeric mice, in which only radio-resistant stromal cells express GFP. Mice received fluorescently labeled anti-Lyve1 and anti-PNAd (MECA-79) to visualize lymphatics and HEVs, respectively. Isolated LNs were cleared with BABB (top) or CUBIC (bottom). The top row shows a single z section, while the bottom row shows the maximum intensity projection (MIP). Stripes in the CUBIC-cleared LN arise from impurities in the agarose block and are unrelated to the clearing protocol used. Scale bar, 130 µm. The insert on the CUBIC-cleared LN shows a the GFP signal from the T cell area –

B cell follicle border highlighted with a white square in the GFP channel of the CUBIC z-section. Scale bar, 20 µm. (D and E) Optical slice of LNs shown in (C) at the axial center (D) and corresponding GFP fluorescence intensity (E). Images show x-y plane. Representative data of six (A and B) or four LNs (C–E) are shown.

Figure 3. GFP-expressing single cell detection in LNs cleared with CUBIC. Mice were s.c. immunized with 2 x 10^4 SIINFEKL-pulsed CellTracker Orange-labeled BMDCs followed by transfer of 1 x 10^4 GFP-expressing OT-I cells. At 48 h post immunization, maximum intensity projection (A) and surface rendered (B) images of the LN after optical clearing with CUBIC are shown. In both images, LN outline (rendered from autofluorescence) and signal of HEV staining are depicted together with OT-I cells (green) and BMDCs (red). The magnified insert shows individual T cells and DCs in the T cell zone. Scale bar, 200 µm. One representative LN of eight LNs is shown.

Figure 4. Quantification of T cell homing into LNs. (A) Representative SPIM-based 3D-volume renderings of HEV network (grey) and fluorescently labelled T cells (green) in LNs 24 h post transfer of increasing number of T cells. Higher magnification image shows rare T cells (yellow arrowheads) in the T cell zone. Scale bar, 150 µm. (B) Total T cell numbers detected in popliteal LNs 24 h post transfer. Each dot represents one LN. (C) Efficacy of T cell homing to popliteal LN as percentage of transferred T cells. Floating bars show minimum and maximum. (D) Representative images showing T cells located intravascular, perivascular or within LN parenchyma 24 h post transfer of 1 x 10^5 T cells. Red arrows point to exemplary T cells at indicated localization. (E) Percentages of cells located intravascular, perivascular or within LN parenchyma. Data are pooled from 4 LNs isolated from mice that received 1 x 10^5 T cells and are shown ± SD. (F) Volume of popliteal LNs after i.v. transfer of increasing number of T cells. Data in B, C, E and F are pooled from 2 independent experiments.

Figure 5. Quantification of DC migration into draining LNs. (A) Representative SPIM-based 3D renderings of HEV network (grey) and DCs (green) in popliteal LNs 24 h post s.c. injection of increasing numbers of fluorescently labelled DCs. Higher magnification image shows rare DCs (yellow arrowheads) in the T cell zone. The red arrow points to the entry point of DCs into the LN. Scale bar, 150 µm. (B) Total DC numbers in draining LNs 24 h post transfer. Each dot represents one LN. (C) Efficacy of DC migration to draining LNs as percentage DC of injected DCs. Floating bars show minimum and maximum. (D) Volume of draining popliteal LNs after s.c. injection of increasing numbers of DCs. Data in B – D are pooled from 2 independent experiments. Statistical significance was analyzed by Kruskal-Wallis test with Dunn`s post test. **, $p < 0.01$.

Figure 6. **Identification of Antigen-driven T cell – DC interactions in entire LNs using SPIM.** (A) Experimental outline. C57BL/6 mice received s.c. injection of low (2×10^4) or high amounts (2×10^5) of DCs pulsed with cognate peptides or left unpulsed. After 18 h, 5×10^4 OT-I and OT-II T cells were adoptively transferred. Draining LNs were isolated 8 h later and processed for SPIM. (B) Representative images of close cellular contacts (red circles) between OT-I T cells (green), OT-II T cells (red) and DC pulsed with cognate peptides (blue). (C) Automated centroid position distance measurements between nearest OT-I or OT-II T cells and pulsed or unpulsed DCs from SPIM-based 3D reconstructions of an entire representative LN containing low amounts of DCs, subdivided into interacting versus non-interacting pairs as assessed by visual inspection of individual distances. The dotted line shows the 20 µm centroid distance threshold. (D) Relationship between number of DCs detected in the LN and percentage of OT-I or OT-II T cells being in close cellular contact with pulsed versus unpulsed DCs after low and high DC transfer. (E) Minimum distances between centroids of individual OT-I or OT-II T cells and DCs in representative LNs containing low or high DC numbers. Red bars represent mean. Data are from two independent experiments and were analyzed with Mann-Whitney Test. ***, $p < 0.001$.

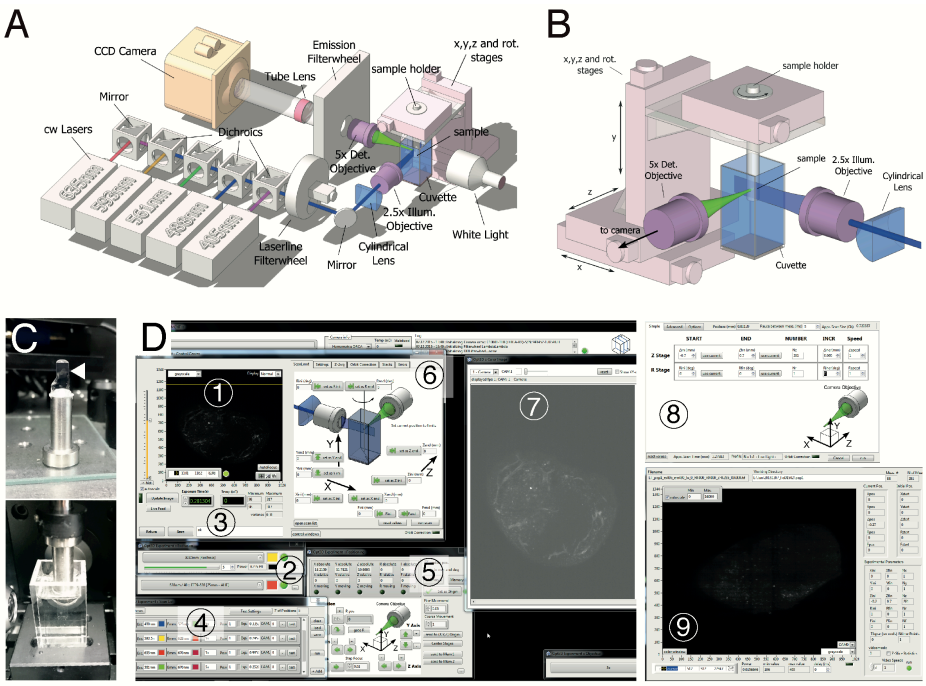
A
CCD Camera
Emission Filterwheel
x,y,z and rot. stages
Tube Lens
sample holder
Mirror
cw Lasers
Dichroics
sample
5x Det. Objective
Cuvette
2.5x Illum. Objective
White Light
Laserline Filterwheel
Mirror
Cylindrical Lens
B
x,y,z and rot. stages
sample holder
y
5x Det. Objective
sample
2.5x Illum. Objective
Cylindrical Lens
z
to camera
Cuvette
x
C
D
1
2
3
4
5
6
7
8
9

Figure 1

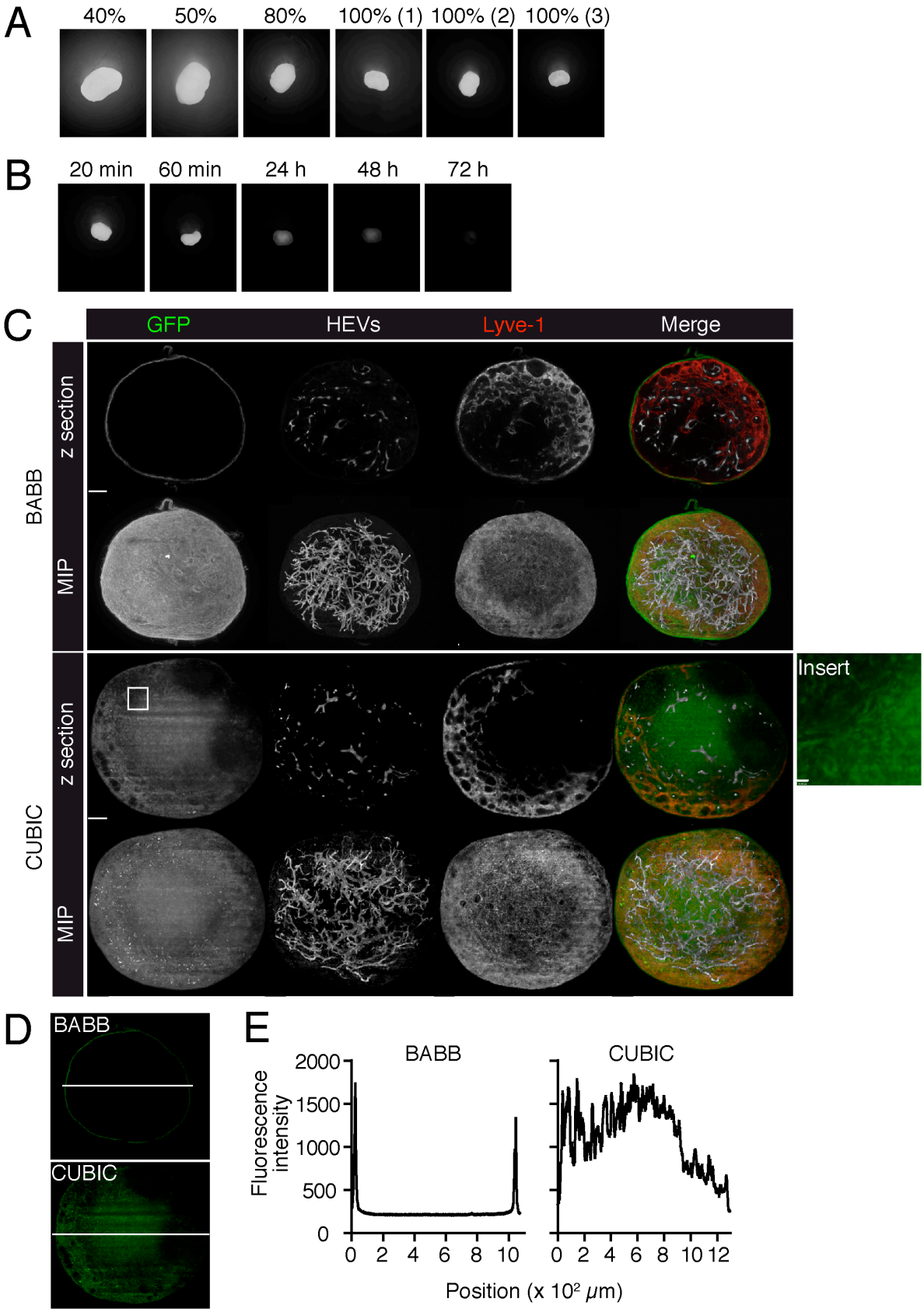
A
40%
50%
80%
100% (1)
100% (2)
100% (3)
B
20 min
60 min
24 h
48 h
72 h
C
GFP
HEVs
Lyve-1
Merge
BABB
z section
MIP
CUBIC
z section
MIP
Insert
D
BABB
CUBIC
E
BABB
CUBIC
Fluorescence intensity
2000
1500
1000
500
0
0 2 4 6 8 10
0 2 4 6 8 10 12
Position (x 10² μm)

Figure 2

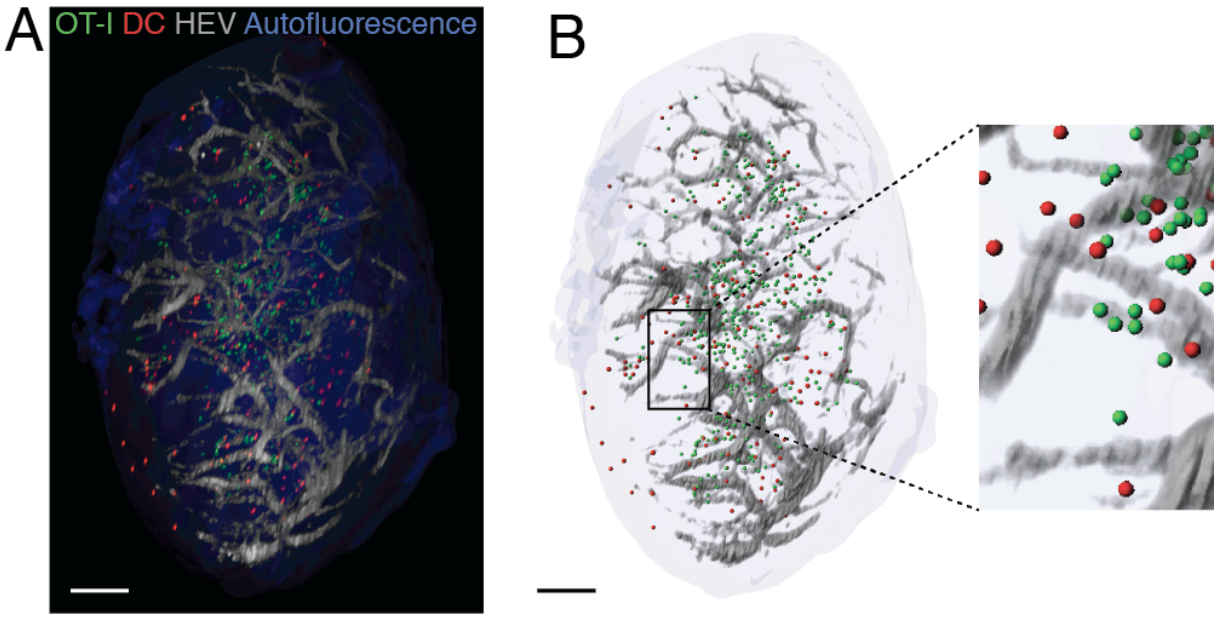

Figure 3

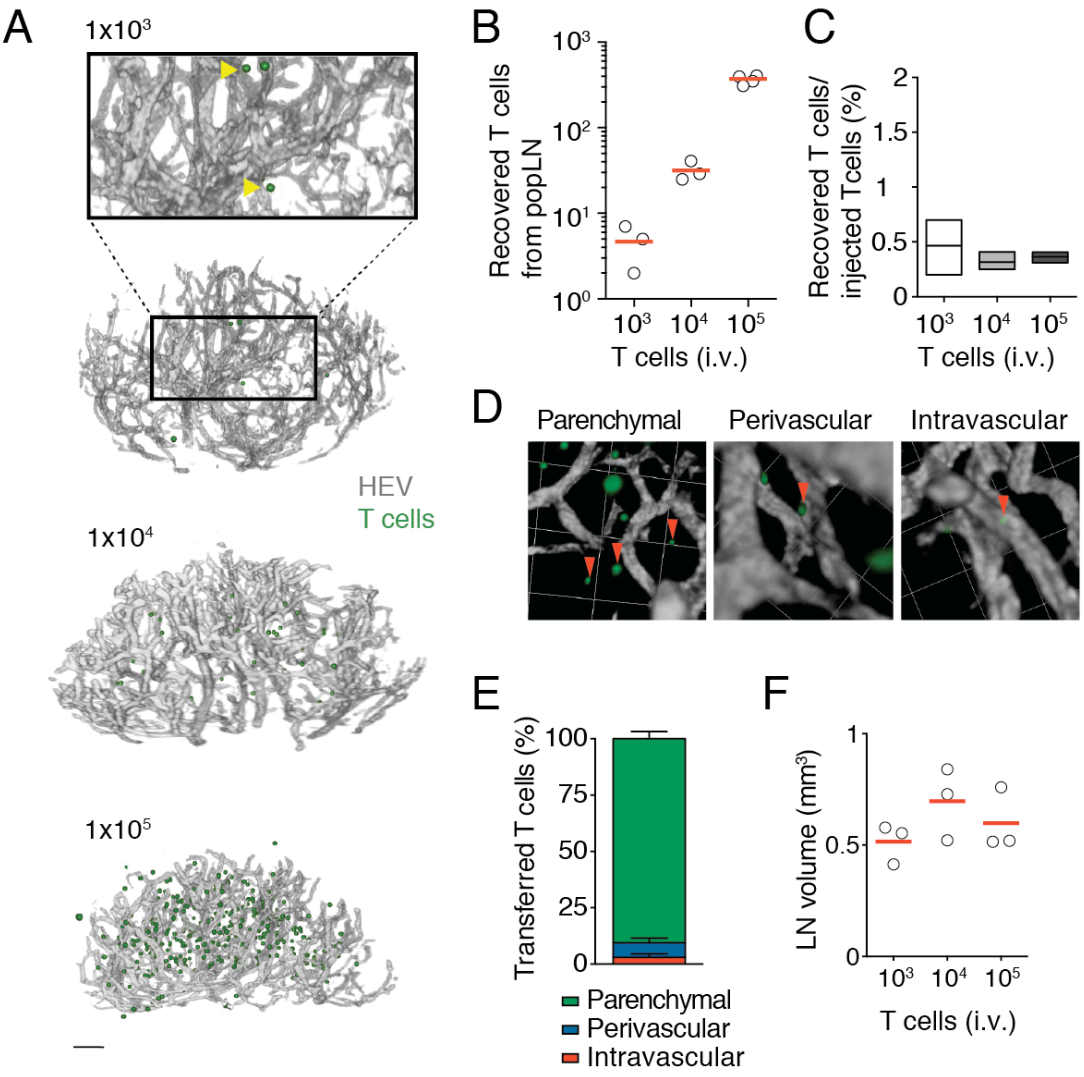
A
1x10³
HEV
T cells
1x10⁴
1x10⁵
B
Recovered T cells from popLN
T cells (i.v.)
C
Recovered T cells/ injected Tcells (%)
T cells (i.v.)
D
Parenchymal
Perivascular
Intravascular
E
Transferred T cells (%)
Parenchymal
Perivascular
Intravascular
F
LN volume (mm³)
T cells (i.v.)

Figure 4

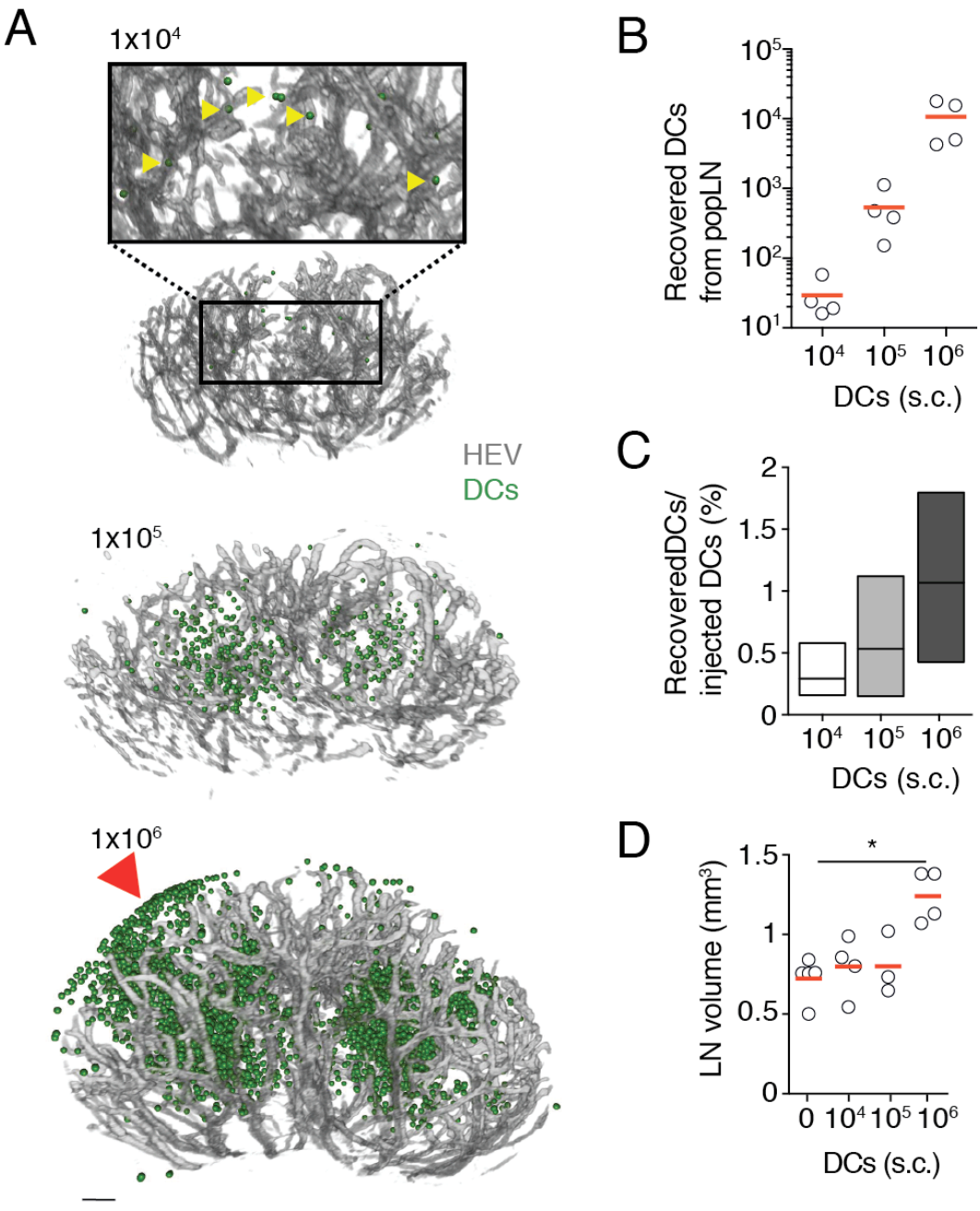
A
1x10⁴
HEV
DCs
1x10⁵
1x10⁶
B
Recovered DCs from popLN
10⁵
10⁴
10³
10²
10¹
10⁴ 10⁵ 10⁶
DCs (s.c.)
C
RecoveredDCs/ injected DCs (%)
2
1.5
1
0.5
0
10⁴ 10⁵ 10⁶
DCs (s.c.)
D
LN volume (mm³)
1.5
1
0.5
0
*
0 10⁴ 10⁵ 10⁶
DCs (s.c.)

Figure 5

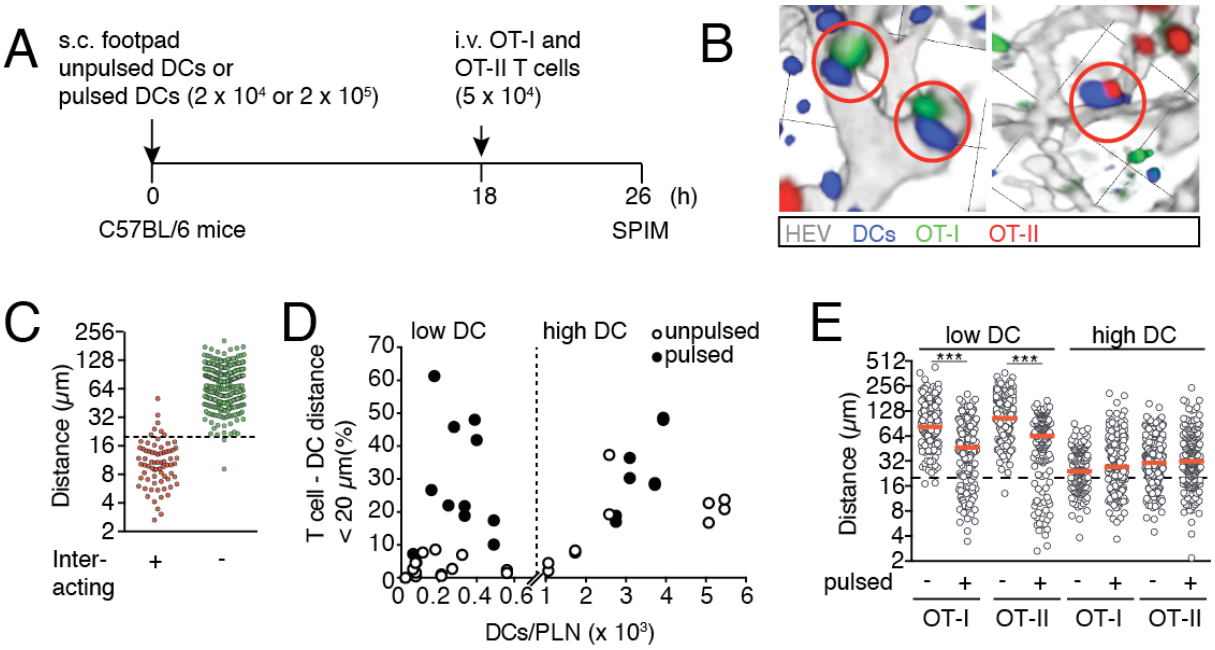
A
s.c. footpad
unpulsed DCs or
pulsed DCs (2 x 10⁴ or 2 x 10⁵)
i.v. OT-I and
OT-II T cells
(5 x 10⁴)
0
18
26 (h)
C57BL/6 mice
SPIM
B
HEV DCs OT-I OT-II
C
Distance (μm)
256
128
64
32
16
8
4
2
Inter-acting
+
-
D
low DC
high DC
unpulsed
pulsed
T cell - DC distance < 20 μm(%)
70
60
50
40
30
20
10
0
0 0.2 0.4 0.6 1 2 3 4 5 6
DCs/PLN (x 10³)
E
low DC
high DC
***
***
Distance (μm)
512
256
128
64
32
16
8
4
2
pulsed
- + - + - + - +
OT-I OT-II OT-I OT-II

Figure 6

Table 1. Comparison of clearing methods for LNs

Method	Composition	FP preservation	Clearing	Compatibility with agarose	Reference
3DISCO	1) THF 2) DBE	+/–	+++	+	(Ertürk et al., 2012)
SeeDB	fructose, a-thioglycerol	+++	+/–	+	(Ke et al., 2013)
ClearT2	formamide, polyethylene glycol	+++	+	–	(Kuwajima et al., 2013)
CUBIC	1) N, N, N', N'-tetrakis-(2-hydroxypropyl)-ethylendiamine, Triton X-100, urea 2) triethanolamine, sucrose, urea, Triton X-100	+++	++	+	(Susaki et al., 2014)